

# Phengite composition and high- pressure metamorphism of the Rheinische Schiefergebirge in the Rhenohercynian belt: implication of phengite in $S_2$ -cleavage

Aung Moe<sup>1</sup>, Kyi Khin<sup>2</sup>

<sup>1</sup>Department of geology, Yangon University, Yangon, Myanmar

<sup>2</sup>Department of Deep Tunnel Sewerage System, National Water Agency, PUB, Singapore

## ABSTRACT

The white K-micas as a phengite ( $Si_{3.2-3.5}$ ) grow an alignment parallel to  $S_2$ -cleavage and high angles to the pre-existing structures, e.g.,  $S_1$ -cleavage and bedding ( $S_0$ ). To confirm phengite, the electron microprobe analysis is carried out in three samples from different localities in the Lahn-Dill areas. The white K-micas are common in the Rheinische Schiefergebirge, the Rhenohercynian belt, known as an accretionary prism. In the world example of accretionary setting phengite micas are transformed at the high anchizone and epizone, which is different from syn-tectonic  $S_1$ -cleavage and late-tectonic  $S_2$ -cleavage of Variscan in the Rhenohercynian belt. Phengite geothermobarometry analysis shows the pressure in 4.5-6.5 kbars and the temperature in 300 °C. The P-T path through lower greenschist to blueschist is manifested in this study. The  $S_2$ -cleavage formed as an  $S_1$ -cleavage kinking due to shear in the  $S_1$ -cleavage which is deduced from the  $S_1$ -cleavage rotations: one anticlockwise due to the collision with London-Brabant Massif and one clockwise due to the dextral shear movement of the Rhenohercynian belt during the late Variscan orogeny.

## KEYWORDS

Rheinische schiefergebirge; Rhenohercynian belt; Phengite;  $S_2$ -cleavage; Dextral shear; Variscan orogeny

## ARTICLE HISTORY

Received 08 January 2025;  
Revised 20 February 2025;  
Accepted 3 March 2025

## Introduction

The white K-mica was coincidentally identified in lime-nodule slates (German: "Kalkknotenschiefer") during the assessment of thin sections by optical petrography. The reddish slates (Upper Devonian) contain lime nodules (German: "knoten") that are well exposed at Weilburg in the Lahn area and different localities in the Dill area (Figure 1). The white mica in the microscopic study was observed as muscovite; however, muscovite is incompatible with low-grade metamorphic rock. Its chemical composition was confirmed in situ by electron-probe micro-analysis (EPMA) on three of the red lime-nodule slate from Weilburg1, Weilburg2, and Dillenburg, which revealed its identity as phengite mica. So far, no phengite mica has been observed in these areas, however, the phengite was already mentioned as a high-pressure mineral in the Northern Phyllite zone, and Southern Taunus Zone, from the south to north in the Rhenohercynian belt [1-4].

White phengite mica has been used as a new barometer, for the Northern Phyllite Zone in the southern part of the Rheinische Schiefergebirge (RS), implying high-grade metamorphic rocks under temperature conditions of 400-450°C and pressure range 10-12 kbar [1,2]. In the RS, the white mica is used for K-Ar and Rb-Sr age determinations by,  $^{40}\text{Ar}/^{39}\text{Ar}$ -dating by, and the metamorphism is generally very low-grade or anchizonal [2,5-8].

In order to study the microstructural analysis of lime-nodule slates, the thin sections were carried out by microscopic analysis. The white mica was unfortunately observed and has to be identified by EPMA. Although the white micas collected from the Lahn-Dill areas are shown as phengite mica, other localities in the RS where the white micas are used in age

dating, are not sure whether they are phengite or not, as they have not been analyzed yet in the electron microprobe study.

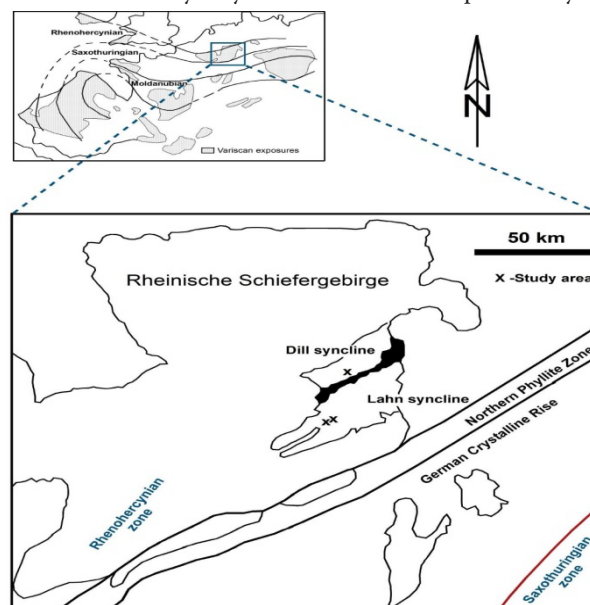


Figure 1. Location map of study points in Lahn-Dill areas

## Analytical Methods

### Sample collection and optical petrography

Lime-nodule slate samples were collected from a number of outcrops (Weilburg1 = 50°28'24.52''N, 8°15'54.67''E;

\*Correspondence: Aung Moe, Department of geology, Yangon University, Yangon, Myanmar, 11181, e-mail: [amoe1975@gmail.com](mailto:amoe1975@gmail.com)

© 2025 The Author(s). Published by Reseapro Journals. This is an Open Access article distributed under the terms of the Creative Commons Attribution License (<http://creativecommons.org/licenses/by/4.0/>), which permits unrestricted use, distribution, and reproduction in any medium, provided the original work is properly cited.

Weilburg2 = 50°28'24.52''N, 8°15'54.67''E; Dillenburg = 50°44'19.79''N, 8°17'11.04''E), (Figures 1 and 2) by the author during fieldwork. Billets for thin sectioning were cut from the bulk samples using a water-cooled diamond blade at three different orientations to the schistosity, mounted with epoxy to a carrier glass. Standard-sized thin sections 26x46 mm at 30 µm nominal thickness for optical petrography were prepared using silicon carbide paper up to 1 200 mesh fineness (<10 µm), and finished with a 0.17 mm cover glass. One thin section was left uncovered and instead, its surface was polished using diamond paste 6310.25 µm on cloth, to achieve a mirror finish.

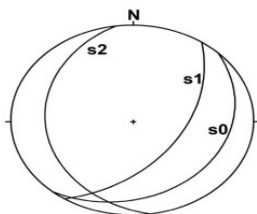


**Figure 2.** S<sub>2</sub>-cleavage developed as high angles to the pre-existing structures of S<sub>1</sub>-cleavage and bedding (S<sub>0</sub>) (Photo: looking SW, 50°28'24.52''N, 8°15'54.67''E).

Finalized sections were studied in a petrographic microscope using plane and cross-polarized transmitted light, to identify mineral phases and (estimated) modal contents (in vol%), and to determine microstructure, texture/fabric, deformation history, and their interrelations. The polished section selected locations suitable for subsequent micro-analysis, with well-defined mineral grain boundaries, immaculate surface finish (plane, no scratches), and without solid or fluid inclusions.

### Mineral chemistry by electron-probe micro-analysis (EPMA)

Prior to analysis, the polished section was coated with 20 nm of carbon in a Polaron CC7650 thermal coater. Pre-selected spots were analyzed by EPMA at high vacuum (<5•10<sup>-6</sup> Torr) in a Cameca SX51 instrument, operated at 15 kV acceleration voltage and ~20.0 nA probe current, equipped with five wavelength-dispersive spectrometers (WDS) and one energy-dispersive spectrometer (EDS). The instrument was internally calibrated against a set of natural and synthetic mineral compounds.

Spectra were acquired for 30s on the peak, and 10s on the background. All elements were measured on their respective K α lines. Sodium Na was assigned to two opposing WDS spectrometers at the beginning of each analytical run to minimize migration effects. Raw element data were ZAF

corrected using the PAP algorithm of, and converted to weight percentages (wt%) of element oxides assuming stoichiometry [9]. FeOT represents total iron (oxide) content, whereas hydrous species contents (H<sub>2</sub>O<sup>+</sup>, H<sub>2</sub>O) were reverse calculated. Net lower limits of detection (LLD) are on the order of 0.0x wt% as specified per element (oxide) in Tables 1 to 4.

Weight percentages of oxides were recast into numbers of cations in atoms per formula unit (apfu) following instructions in the Appendices to, and mica compositions were classified according to the IMA-approved scheme of [10,11]. Selected results are collated in Tables 2, 3, and 4.

### X-ray powder diffraction (XRPD) analysis

To assist in the identification of the fine-grained matrix material and the nature of the white micas observed in thin sections, pre-crushed bulk sample materials were pulverized under acetone in an agate mortar and pestle, to pass a 200-mesh sieve (<75 µm). Dried and homogenized powders were loaded in a dimpled aluminum sample holder and finished with a microscope carrier glass to obtain a flat surface.

Powder diffractograms were recorded in a Bruker D8 Advance X-ray diffractometer (XRD) instrument with Bragg-Brentano geometry from 02 23 °2θ in 0.05 °2θ steps, with 30 s per step, overall scan time 3h30m per sample. The Cu-tube was operated at 40 kV and 40 mA and produced bulk (non-monochromatic) CuKα radiation of λ=1.54184 Å. CuKβ was removed from the diffracted beam with Ni-foil. Peaks were indexed with DIFFRAC.EVA V4.2 proprietary Bruker software using the ICDD 4.0 database. Selected results are collated in Figure 7.

## Results

### Optical thin section petrography

The mineral assemblage of quartz, chlorite, and white mica was observed in the petrographic analysis of the red lime-nodule slate. Quartz usually is present as lenticular grains, and chlorite in the form of overgrowths on it. The phengite micas show an alignment that is neither parallel to the S<sub>1</sub>-cleavage nor bedding (S<sub>0</sub>), but transverse to the S<sub>1</sub>-cleavage, whereas S<sub>1</sub>-cleavage consists of lenticular quartz, chlorite, and mica (muscovite). The alignment of a possible S<sub>2</sub>-cleavage consists of phengite mica, quartz (small grains), and chlorite (Figures 2, 3).

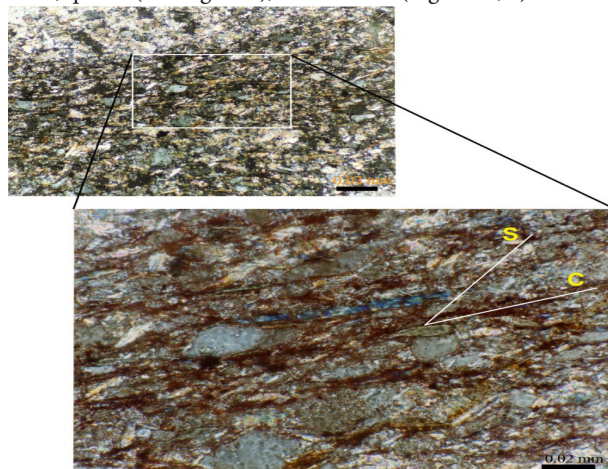


**Figure 3.** Microphotographs in cross-polarized light (XPL) showing the S-C fabrics with lenticular quartz and lithic fragments, and mica minerals from the large scale. The elongated blue colour strip is a chlorite flake.

### Mineral chemistry

Of the twenty-seven randomly selected points from three localities, sixteen are phengite and eleven are muscovite or illite. Phengite grows at an angle to the S<sub>1</sub>-cleavage whereas muscovite or illite grows parallel to the S<sub>1</sub>-cleavage (Figure 4).

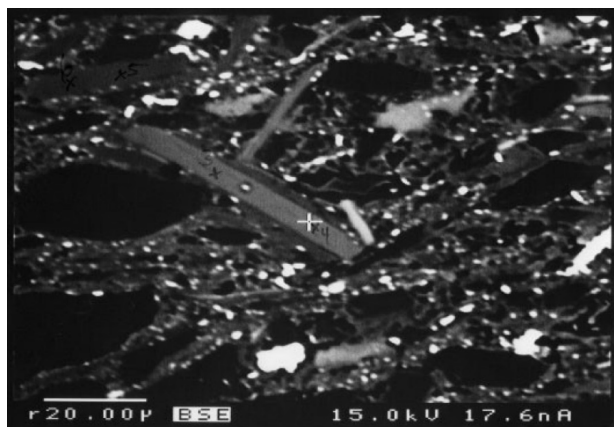


**Figure 4.** EPMA microphotograph (back-scattered electron – BSE image) revealing lenticular quartz (black holes), tiny opaque phases (white) in a fine-grained matrix (dark grey), and a zoned phyllosilicate grain overgrowing the fabric (pale grey). The cross-hairs at the centre indicate a spot for EPMA analysis.

These micas, i.e., illite, phengite and muscovite are generally determined by the SiO<sub>2</sub> and Al<sub>2</sub>O<sub>3</sub> content (wt%) (see Figure 5 and Table 1) [12-15].

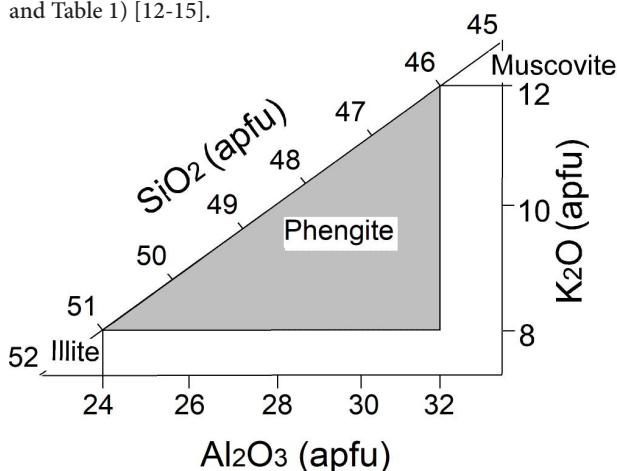


**Figure 5.** Diagram of SiO<sub>2</sub>-Al<sub>2</sub>O<sub>3</sub>-K<sub>2</sub>O for illite, phengite, and muscovite classification.

**Table 1.** Main element oxide contents in illite, phengite, and muscovite from the published literature. Illite, phengite, and muscovite were analyzed by EPMA.

	illite*	phengite†	muscovite‡	nominal
<i>main element oxide contents in weight percent (wt%)</i>				
SiO <sub>2</sub>	51.25	48.89	45.55	45.26
TiO <sub>2</sub>	0.17	0.08	0.26	0.00
Al <sub>2</sub> O <sub>3</sub>	23.53	26.80	36.89	38.40
Fe <sub>2</sub> O <sub>3</sub>	2.02	n.a.	0.39	0.00
FeO	0.33	3.62	0.86	0.00
MnO	n.a.	0.02	0.02	0.00

MgO	3.32	2.99	0.58	0.00
CaO	0.59	0.08	0.04	0.00
Na <sub>2</sub> O	0.05	0.14	0.80	0.00
K <sub>2</sub> O	7.61	10.05	10.17	11.82
H <sub>2</sub> O <sup>+</sup>	5.87	n.a.	0.03	0.00
H <sub>2</sub> O <sup>-</sup>	5.26	n.a.	4.59	4.52
total	100.02	93.21	100.18	100.00
<i>cations in atoms per formula unit (apfu) based on 100</i>				
Si	7.163	6.729	6.040	3.000
Al	0.837	1.271	1.960	1.000
ΣZ	8.000	8.000	8.000	4.000
Al	3.040	3.077	3.800	2.000
Ti	0.018	0.018	0.020	0.000
Fe <sup>3+</sup>	0.212	0.417	0.040	0.000
Fe <sup>2+</sup>	0.038	0	0.100	0.000
Mn	0	0.002	0	0.000
Mg	0.692	0.614	0.120	0.000
ΣY	4.000	4.130	4.080	2.000
Ca	0.088	0.012	0	0.000
Na	0.014	0.037	0.200	0.000
K	1.357	1.844	1.720	1.000
ΣX	1.460	1.890	1.920	1.000
OH	4.000	0	1.990	2.000

\* from [12], (p359)† from [13], (p164), calculated average (n=7)‡ from [15], (p1360)

Park showed the major elements of the typical phengite-series compositions ranging as 44.50–55.86 wt% for SiO<sub>2</sub>, 21.05–36.87 wt% for Al<sub>2</sub>O<sub>3</sub>, 10.60–11.67 wt% for K<sub>2</sub>O, 0.00–7.01 wt% for MgO and almost 0.00 wt% for FeO [16].

Therefore, phengite is defined in this study as follows:

SiO<sub>2</sub> content of illite is more than that of phengite and more than that of muscovite.

51 > phengite > 49

Al<sub>2</sub>O<sub>3</sub> content of illite is less than that of phengite and less than that of muscovite.

24 < phengite < 32

K<sub>2</sub>O content is variable, however, it can be defined as,

8 < phengite < 12

K<sub>2</sub>O content of illite to muscovite is different between their origin, e.g., K<sub>2</sub>O % illite to muscovite in anchimetamorphic zone = 8.6 - 10.2 wt% and K<sub>2</sub>O % illite to muscovite in epimetamorphic zone = 9.9 - 11.4 wt% [13,14].

In addition, the Si<sup>+</sup> and Al<sup>+</sup> diagram is used to define the phengite (celandonic muscovite; proposed by in the solid solution of celadonite-muscovite after which fit into the metamorphic facies [13,17-20]. The celadonite-muscovite relationships (Figure 6) show that none of the white mica plots are considered ideal muscovite and 16 of them are enriched in the celadonite component. Thus, the celadonite and phengite contents are not independent of each other but increase together [21]. Additionally, the total value of Ca<sup>+</sup>, Na<sup>+</sup>, and K<sup>+</sup> can also be used to determine the phengite, for which the range between 1.65 and 2.00 is defined (Tables 2, 3, and 4), in which K<sup>+</sup> values are higher than Na<sup>+</sup> values.

**Table 2.** Main element oxide contents by EPMA in weight percent (wt%) in phengite from Weilburg, in the middle Lahn syncline. FeOT represents total iron (oxide) content, and H<sub>2</sub>O is reverse-calculated by stoichiometry.

sample	1	2	3	4	5	6	7	8	9	10	
<b>oxide</b>	<b>LLD</b>	<i>main element oxide contents in weight percent (wt%)</i>									
SiO <sub>2</sub>	0.50	45.51	52.64	51.18	50.65	48.18	48.35	50.47	50.07	47.77	48.92
TiO <sub>2</sub>	0.01	0.35	0.24	0.38	0.42	0.40	0.27	0.33	0.44	0.49	0.58
Al <sub>2</sub> O <sub>3</sub>	0.02	31.58	27.74	26.46	25.87	33.98	35.75	25.02	24.85	34.09	34.45
Cr <sub>2</sub> O <sub>3</sub>	0.01	<LLD	0.05	<LLD	<LLD	<LLD	0.03	0.02	0.02	0.05	<LLD
FeO <sup>T</sup>	0.01	2.71	3.87	5.86	6.04	1.70	1.28	7.41	6.91	1.60	1.54
MnO	0.01	0.01	0.04	0.07	0.08	<LLD	0.02	0.06	0.08	0.01	0.04
MgO	0.04	1.58	2.49	2.57	2.64	1.02	0.57	2.84	2.83	1.05	1.12
CaO	0.01	<LLD	0.08	<LLD	0.01	<LLD	0.02	0.01	<LLD	0.02	<LLD
Na <sub>2</sub> O	0.10	0.38	0.18	0.22	0.20	0.92	1.05	0.09	0.05	0.69	0.70
K <sub>2</sub> O	0.01	9.37	8.17	9.34	9.79	9.47	8.68	9.42	9.207	8.31	8.75
H <sub>2</sub> O	0.25	4.48	4.55	4.49	4.45	4.55	4.60	4.35	4.39	4.51	4.50
total	98.99	100.05	100.58	100.15	100.33	100.63	100.02	99.35	98.59	100.68	
		<i>numbers of cations in atoms per formula unit (apfu) based on 100</i>									
Si		6.494	6.930	6.839	6.829	6.357	6.300	6.952	6.840	6.351	6.375
Al <sup>IV</sup>		1.506	1.072	1.181	1.170	1.643	1.600	1.049	1.160	1.649	1.625
	ΣZ	8.000	8.000	8.000	8.000	8.000	8.000	8.000	8.000	8.000	8.000
Al <sup>VI</sup>		3.477	3.230	3.006	2.942	3.629	3.791	3.013	2.842	3.693	3.666
Cr		0	0.005	0	0	0	0.003	0.002	0.002	0.006	0
Ti		0.035	0.024	0.038	0.043	0.040	0.027	0.034	0.046	0.049	0.056
Fe		0.304	0.426	0.655	0.682	0.187	0.140	0.718	0.789	0.178	0.168
Mn		0.002	0.005	0.008	0.009	0	0.002	0.006	0.010	0.002	0.004
Mg		0.315	0.489	0.512	0.531	0.201	0.112	0.584	0.576	0.207	0.217
	ΣY	4.133	4.179	4.219	4.207	4.058	4.074	4.356	4.265	4.134	4.112
Ca		0.001	0.011	0	0.001	0.001	0.002	0.002	0	0.003	0
Na		0.059	0.047	0.058	0.053	0.236	0.265	0.024	0.015	0.177	0.176
K		0.600	1.372	1.592	1.683	1.589	1.443	1.654	1.688	1.410	1.454
	ΣX	0.660	1.430	1.650	1.737	1.825	1.710	1.678	1.704	1.590	1.630

**Table 3.** Main element oxide contents by EPMA in weight percent (wt%) in phengite from Weilburg, in the middle Lahn syncline. FeOT represents total iron (oxide) content, and H<sub>2</sub>O is reverse-calculated by stoichiometry.

sample	1	2	3	4	5	6	7	
<b>oxide</b>	<b>LLD</b>	<i>main element oxide contents in weight percent (wt%)</i>						
SiO <sub>2</sub>	0.50	50.72	48.51	50.24	46.78	51.06	48.07	47.46
TiO <sub>2</sub>	0.01	0.43	0.27	0.41	0.22	1.01	0.12	0.47
Al <sub>2</sub> O <sub>3</sub>	0.02	26.08	25.31	24.29	31.33	22.70	25.71	27.31

Cr <sub>2</sub> O <sub>3</sub>	0.01	<LLD	0.03	0.02	<LLD	<LLD	0.04	0.03
FeO <sup>T</sup>	0.01	4.35	4.07	6.88	1.61	5.00	5.12	3.26
MnO	0.01	<LLD	0.04	0.05	0.02	0.09	0.08	0.02
MgO	0.04	2.89	3.60	4.27	1.03	3.92	2.82	2.26
CaO	0.01	0.08	2.15	0.25	0.13	0.32	0.12	0.17
Na <sub>2</sub> O	0.10	0.12	0.16	0.26	0.49	0.14	0.28	0.57
K <sub>2</sub> O	0.01	9.11	8.22	7.87	9.72	8.59	9.69	10.14
H <sub>2</sub> O	0.25	4.43	4.33	4.42	4.34	4.37	4.29	4.29
	total	98.28	96.76	99.07	95.68	97.29	96.41	96.03
<i>numbers of cations in atoms per formula unit (apfu) based on 100</i>								
Si		6.870	6.714	6.814	6.468	7.014	6.724	6.630
Al <sup>IV</sup>		1.130	1.286	1.186	1.532	0.986	1.276	1.370
	ΣZ	8.000	8.000	8.000	8.000	8.000	8.000	8.000
Al <sup>VI</sup>		3.034	2.842	2.698	3.576	2.690	2.964	3.126
Cr		0	0.002	0.002	0	0	0.004	0.004
Ti		0.044	0.028	0.042	0.022	0.104	0.012	0.050
Fe		0.494	0.470	0.782	0.516	0.574	0.600	0.382
Mn		0	0.004	0.006	0.002	0.010	0.010	0.002
Mg		0.584	0.742	0.864	0.212	0.802	0.588	0.470
	ΣY	4.156	4.088	4.394	4.328	4.180	4.178	4.034
Ca		0.012	0.320	0.036	0.018	0.048	0.018	0.026
Na		0.032	0.044	0.068	0.130	0.038	0.074	0.154
K		1.574	1.452	1.362	1.714	1.506	1.728	1.808
	ΣX	1.618	1.816	1.466	1.862	1.592	1.820	1.988

**Table 4.** Main element oxide contents by EPMA in weight percent (wt%) in phengite from Eibach (Dillenburg), in the Dill syncline. FeOT represents total iron (oxide) content, H<sub>2</sub>O reverse-calculated by stoichiometry.

oxide	sample	1	2	3	4	5	6	7	8	9	10
	LLD	<i>main element oxide contents in weight percent (wt%)</i>									
SiO <sub>2</sub>	0.50	50.38	47.81	47.53	49.76	49.34	48.52	49.09	47.04	46.72	47.34
TiO <sub>2</sub>	0.01	0.32	0.94	0.05	0.27	0.57	0.16	0.19	0.33	0.39	0.36
Al <sub>2</sub> O <sub>3</sub>	0.02	23.59	24.57	33.65	26.83	25.67	28.47	27.80	34.34	31.21	31.98
Cr <sub>2</sub> O <sub>3</sub>	0.01	0.19	<LLD	0.01	<LLD	<LLD	0.01	0.06	0.05	0.02	<LLD
FeO <sup>T</sup>	0.01	3.20	5.88	1.09	4.31	4.26	3.201	3.34	1.00	2.07	1.75
MnO	0.01	<LLD	0.21	0.01	<LLD	0.05	0.05	0.01	0.03	0.03	<LLD
MgO	0.04	3.02	2.87	0.77	1.84	0.37	1.89	1.88	0.70	1.00	0.89
CaO	0.01	0.07	0.03	0.03	0.01	0.04	0.02	0.16	0.04	0.04	0.02
Na <sub>2</sub> O	0.10	0.12	0.15	0.53	0.53	0.17	0.58	0.56	0.38	0.53	0.47
K <sub>2</sub> O	0.01	9.70	9.72	7.95	9.53	10.34	9.70	9.78	7.50	9.36	8.14
H <sub>2</sub> O	0.25	4.28	4.27	4.204	4.38	4.26	4.36	4.37	4.43	4.34	4.37
	total	98.99	94.91	96.52	96.05	97.54	95.13	96.95	97.27	95.86	95.72
<i>numbers of cations in atoms per formula unit (apfu) based on 100</i>											
Si		7.064	6.718	6.440	6.816	6.952	6.668	6.732	6.368	6.460	6.496
Al <sup>IV</sup>		0.936	1.282	1.560	1.184	1.048	1.332	1.268	1.632	1.540	1.504
	ΣZ	8.000	8.000	8.000	8.000	8.000	8.000	8.000	8.000	8.000	8.000
Al <sup>VI</sup>		2.962	2.786	3.812	3.148	3.214	3.280	3.224	3.846	3.546	3.668
Cr		0.022	0	0.002	0	0	0.002	0.006	0.006	0.002	0

Ti	0.034	0.098	0.006	0.028	0.060	0.016	0.020	0.034	0.040	0.036
Fe	0.374	0.692	0.122	0.494	0.502	0.362	0.384	0.112	0.240	0.020
Mn	0	0.024	0.002	0	0.006	0.006	0	0.002	0.004	0
Mg	0.630	0.600	0.154	0.376	0.078	0.386	0.384	0.142	0.206	0.182
ΣY	4.022	4.200	4.098	4.046	3.860	4.052	4.018	4.142	4.038	3.906
Ca	0.010	0.004	0.004	0.002	0.006	0.002	0.022	0.006	0.006	0.002
Na	0.032	0.040	1.380	0.142	0.046	0.154	0.148	0.100	0.142	0.124
K	1.734	1.742	1.374	1.666	1.858	1.700	1.712	1.296	1.652	1.426
ΣX	1.776	1.786	1.516	1.810	1.910	1.856	1.882	1.402	1.800	1.552

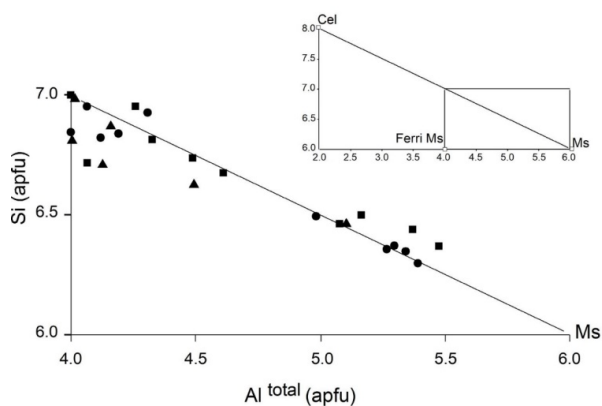


**Figure 6.** Si-Altotal diagram showing celadonite-muscovite solid solution [13], [18], [19]. circles=Weilburg1, triangles=Weilburg2, squares=Dillenburg

### X-ray powder diffraction (XRPD) analysis

The X-ray powder diffraction pattern comprises thousands of overlapping peaks, however, refining the structures of the constituent minerals from overlapping peaks by plots the  $2\theta$  and  $d$  values. Therefore, to detect the minerals, an XRD analysis is carried out on five red slate samples from the Lahn-Dill areas, with the  $2\theta$  and  $d$  values being measured according to the interpretation of Frey, Ehlers & Blatt, and Raudsedd et al [22-24]. In the X-ray diffraction pattern, minerals such as phengite, chlorite, quartz, albite,  $\pm$  microcline are recognized in sharp peaks (Figure 7).

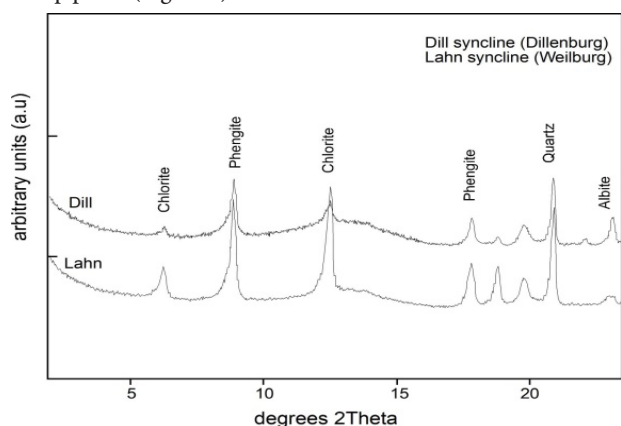


**Figure 7.** XRPD diffractogram stack (arbitrary units: a.u) for red slates (Rotschiefer or Kalknotenschiefer) from the Lahn-Dill area, Rhenohercynian zone. Peak indicators cf. ICDD 4.0 database.

Frey proposed a reaction for the clay minerals to low-grade metamorphic minerals: mixed layer illite/montmorillonite = Al-rich chlorite + phengite + quartz +  $H_2O$ -----(1)[22].

This product assemblage replaces illite in deep diagenesis and anchizonal metamorphism [25,26]. However, Frey and Robinson suggest that the phengite-poor composition and development in the bedding parallel microfabrics may be partly a measure of reaction progress rather than of the pressure [27].

### Metamorphic P, T-Conditions

Velde found Si contents of 3.3 apfu in the solid solution of celadonite + muscovite + phengite in the P-T condition of 250–550 °C and an upper-pressure limit in the range of 8–10 kbar [20].

In the present study, phengite Si contents of 3.4 to 3.5 apfu in the celadonite+muscovite solid solution series indicate the pressure 5-6.5 kbars by the Si-isopleths of phengite in Massonne and Schreyer, and compared to Franz et al., and the temperature 250-350 °C through the lower limit of greenschist and the upper limit of biotite absence, (Figure 3) [28-30]. Phengite thermometer for the P-T path of this study area can be estimated from sub-greenschist to blueschist in the clockwise pattern (Figure 8).

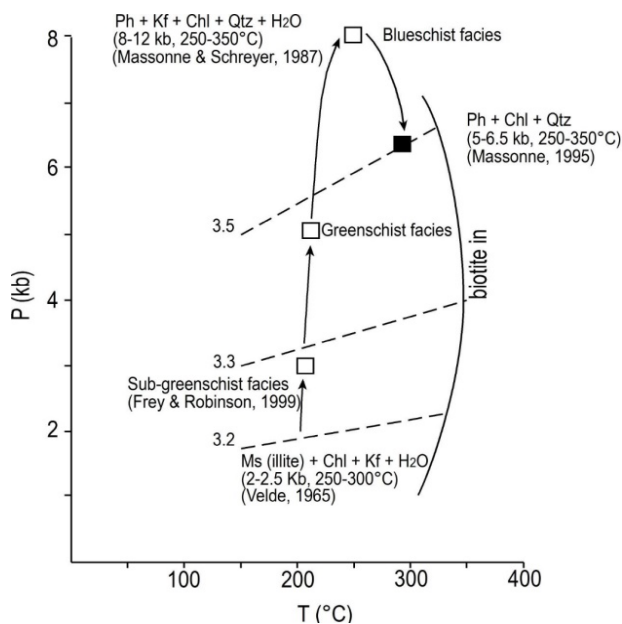
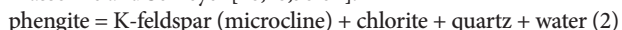


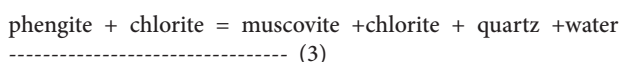
**Figure 8.** P-T path for the Lahn-Dill area. black square=study area, square=pre-stages

The mineral assemblage of the S<sub>2</sub>-cleavage consisting of phengite mica, quartz, and chlorite is transformed from the mineral assemblage of the S<sub>1</sub>-cleavage. Possible reactions are proposed based on previous work in the field of biotite absence, e.g., who introduced the involving of phengite in blueschists as an applicable barometer with the reaction of Velde, Bucher-Nurminen and Massonne and Schreyer [20,28,30-32]:

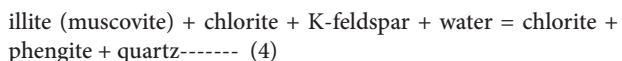


Above the equilibrium condition, the phengite barometer is applied to the presence of K-feldspar [27]. Essene Pointed out that the phengite barometer provides only minimum limits of pressure in the absence of the K-feldspar [31].

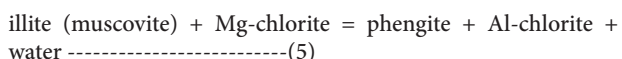
Thus, a reaction in the greenschist facies within the biotite absence field can be proposed:



Velde proposed the very probable reaction in a series of sedimentary rocks at low temperature and high pressure, which can be compared with the modelling of Zhu and Wei [20,33]:



Holland and Lambert used a reaction for the pelitic rocks in the low temperature (200-400 °C) metamorphic regime [34]:



Therefore, there is no evidence of phengite used as a geobarometer at high temperatures (T > 750°C) [35]. The white mica is more similar to the ideal composition of muscovite. Phengite has higher SiO<sub>2</sub> and lower Al<sub>2</sub>O<sub>3</sub> than muscovite and contains significant amounts of MgO, FeO and Fe<sub>2</sub>O<sub>3</sub>. Again, Tilley and Ernst observed that the white micas of low-grade muscovite-chlorite and glaucophane schists usually contain significant amounts of MgO, FeO, and Fe<sub>2</sub>O<sub>3</sub>, and are therefore called phengite [36,15].

Velde has presented some preliminary data on the experimental conversion of quartz-bearing sedimentary montmorillonite and illite assemblages into metamorphic mixtures of quartz, white mica, and chlorite [37]. At PH<sub>2</sub>O = 2 kb, he places such reactions in the vicinity of 300 °C, marking the appearance of what might be called a greenschist assemblage text in [38,39]. Low temperatures and high pressures are found to favour the transition of phengite micas from muscovite toward celadonite, rather than to near-ideal muscovite.

The lower stability limit of metamorphic muscovite (white mica) - chlorite - quartz assemblages of the greenschist facies is around T = 300 °C and PH<sub>2</sub>O = 3 kb, possibly somewhat lower [38]. However, Massonne and Schreyer found the stability field of the phengite - K-feldspar - quartz assemblage in the excess H<sub>2</sub>O between < 350 °C and upper-pressure limit in the range of 8 - 12 kbars within the upper limit of biotite absence zone [28].

### Metamorphism of the Rheinische Schiefergebirge Regional metamorphism

The metamorphism of the Rheinische Schiefergebirge gradually died out towards the north with syntectonic folding and its

associated first cleavage (S<sub>1</sub>) [6,40,41]. The S<sub>2</sub>-cleavage (crenulation cleavage) as encountered in the RS shows the same deformation fabric as the post-crystalline form of the first cleavage [40-42].

The temperature does not exceed 350 °C, and most places range 200-300°C, except in the Taunus, where it reaches 400-450°C, compared to (cf.) [6,39].

### White mica

White mica is well distributed as a metamorphic mineral in the RS from the Northern Phyllite Zone in the south to Ostsauerland in the north. Its distribution is based on K-Ar and Rb-Sr age determinations by Ahrendt et al. and 40Ar/39Ar-dating by Fladt et al. [5,2].

In the SW Moselle region, Hoepfener stated that the white mica that lens shape fine chlorite and sericite flakes are smaller than 10 μ in diameter, and large individual minerals such as chlorite, white mica, and quartz are about 20 μ in diameter [43].

In the Hunsrückschiefer of the middle Moselle region, Talbot observed that an aggregate of quartz, white mica, and chlorite is common with white mica also occurring in grains of comparable size to the quartz, but more commonly from slightly larger aggregates (lenticular) with chlorite [44]. In this region, Hoepfener concluded that the lenticulars are formed contemporaneously with the cleavage by overgrowths of the chlorite and mica on sedimentary grains [43].

In pyrophyllite-bearing slates of Ramsbeck, the Ostsauerland region, has found white mica aggregates with syntectonic metasomatism in hydrothermally influenced areas, consisting of pyrophyllite and mica which cooling of the white-mica-stable liquid results in pyrophyllite (± diaspore) becoming stable [45,46].

### White K-mica in the S<sub>2</sub>-cleavage plane

In the field observations, the crenulation cleavage shows a macroscopically distinguishable cleavage lamellae and wider spacing of cleavage planes. The first cleavage takes over the bedding plane, whereas the crenulation cleavage leads to the previous syn-crystalline cleavage (S<sub>1</sub>-cleavage). Thus, crenulation cleavage deformation shows a post-crystalline form of the first cleavage, which is transverse to earlier structures of S<sub>1</sub> and S<sub>0</sub> (cf.) [40,42,44]. The transverse cleavage planes on the fold limbs are interpreted as antithetic shear planes (cf. and S<sub>1</sub>-cleavage planes are related to synthetic shear planes (Figure 9)[40,42].

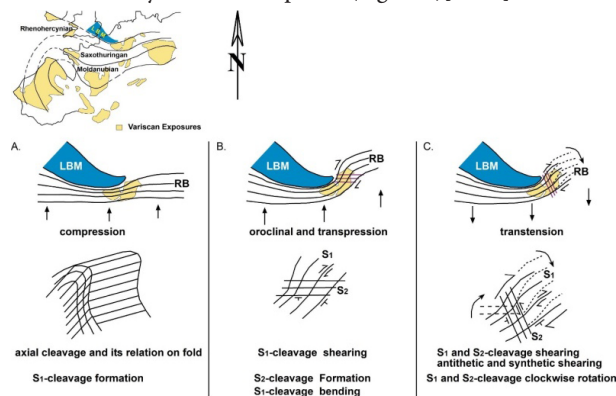


Figure 9. S<sub>1</sub> and S<sub>2</sub> cleavage formation and their related tectonic movement.

In the statement of Weber, the transverse cleavage of the microscopic and macroscopic nature depends primarily on (1) the nature and degree of the pre-existing anisotropy and (2) the relative age of the deformation and crystallization of the mineral phases, which produce that cleavage, whereas that cleavage is generated by the stress direction ( $\sigma_1$  direction) together with the style of tectonic motion, discussed below (Tectonic interpretation) [42].

The  $S_2$ -cleavage cuts at a high angle to the  $S_1$ -cleavage in many places. The angle between  $S_1$  and  $S_2$  in the outcrop varies considerably, ranging from  $10^\circ$  to  $85^\circ$ , with most between  $15^\circ$  and  $60^\circ$  and the mean being around  $35^\circ$ . In the microscope, the angle is relatively less than that of in outcrop. Talbot suggested that the angles between  $S_1$  and  $S_2$  are not primary as a result of later rotation [44]. Similarly,  $S_2$ -fabrics are clearly and continuously visible to better define the crenulation type in the thin section. The fabrics of  $S_1$  and  $S_2$  are very similar to the fabrics of S-C mylonite (Figure 3), which suggests the dynamic effect of the shear zone movement [47-49].

### Structural and Tectonic interpretation

The tectonic movement history of the Rhenohercynian belt is established by the formation of the  $S_1$  and  $S_2$  cleavages (see Figure 9). The tectonic movement of the study area can be deduced from the following investigations:

Firstly, northward movement resulted in the collision as several mutual aspects are evident in Lower Devonian rocks in the north which show only very small deformation. A pre-folding state is preserved with a preferentially N-S trending extension attributed to the stage of basin development.

Secondly, the  $S_1$ -cleavage formed as an axial plane cleavage in the N-vergence through the buttress of the London-Brabant Massif (LBM) against ongoing northward collisional movement. This stage of folding itself during Carboniferous showing syn-kinematic NNW-directed compression occurs simultaneously in larger thrust zones of penetrative deformation.

Thirdly, the northward movement super-stressed the oroclinal bending around the London-Brabant Massif in the Rhenohercynian belt: an  $S_1$ -cleavage is re-trending (nearly NS)

and  $S_2$ -cleavage formation due to the oroclinal bending around the London-Brabant Massif. The  $S_2$ -cleavage runs transversely to the  $S_1$ -cleavage in the Rheinische Schiefergebirge however, the  $S_2$ -cleavage is parallel to the  $S_1$ -cleavage in the Ardennen, from which the  $S_1$ -cleavages from both areas are correlated, and the  $S_2$ -cleavages are also able to correlate [40,50,51].

Movement patterns in the north late-kinematic clockwise rotation of the stress field are only weakly represented in the south. On the other hand, the clear evidence of an even younger counter-clockwise rotation of the stress field concerns the southern massif [52,53].

During the collision of LBM, the Rhenohercynian belt was laid between LBM and the Saxothuringian zone, so the  $S_2$ -cleavage was formed by the high pressure or the Rhenohercynian belt suffered by high-pressure metamorphism.

Among lime nodules that develop pressure shadows, phengite can be seen in a parallel orientation to the  $S_1$ -cleavage. Wilson observed that the presence of pressure shadows behind phengite that were misoriented at a high angle to the foliation suggests a very irregularity [54]. Rolland et al. also noted that phengite aggregates in the pressure shadow formed at the expense of feldspar porphyroclasts [55]. According to the observations of Stephens et al., there are two mica groups in slates of Clunes from Australia, one parallel and one (detritus mica) oblique to cleavage, with phengite mica alignment having a strong preferred orientation parallel to  $S_1$ -cleavage (cf.) [55,56].

The phengite thermobarometer of Lahn-Dill areas of very low to low-grade metamorphic rocks in an accretionary collisional setting generated by B-type subduction of oceanic crust is different from the accretionary setting of Frey and Robinson and El-Rus et al. (Table 5), whose P-T path goes clockwise through the sub-greenschist to blueschist fields following the uplift [27,57]. In their accretionary setting, e.g., the Southern Uplands of Scotland imbricate thrust system is developed on synchronous burial and metamorphism of strata containing soft sediments deformation and strata disruption and cleavage development, and the metapelitic study showing anchizone rocks includes white K-mica which indicates medium-high pressure facies condition.

**Table 5.** Comparison between the Rheinische Schiefergebirge and Accretionary setting

Rheinische Schiefergebirge – accretionary prism	accretionary setting – [27]
<i>S<sub>1</sub>-cleavage formation</i>	
$S_1$ -cleavage is a prominent NW vergence as a tectonic indicator	$S_1$ -cleavage is parallel to the bedding in both high anchizone and epizone
<i>white K-mica formation</i>	
White K-micas are found in the $S_1$ -cleavage	white K-micas only occur in the upper anchizone and the epizone, indicating the inherited pattern as the higher grade in older rocks
White K-micas are found in the Upper Devonian rocks (low anchizone).	Metamorphic grades do not depend on the structures, such as imbrications or duplex thrust systems.

The RS is an N-S transverse complete section of the Rhenohercynian belt, which is well known as an accretionary prism in the Variscan orogen (Figure 10), [45,58,59].

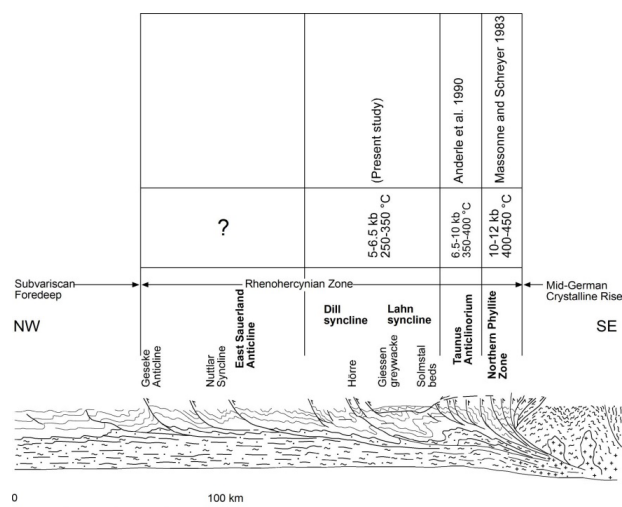


**Figure 10.** P-T condition on the Rhenohercynian zone of the deformation crust from SE to NW. (cross-section: adopted from Weber referred to (ETH)-Zürich) [61,62].

The formation of the same fabric types  $S_1$  and  $S_2$  cleavages can be considered as formation in the relationship of deformation stresses in the rocks. Talbot suggested that the two fabrics are similar and should be treated genetically [44]. Likewise, the development of cleavage is related to a shortening direction and is perpendicular to the cleavage.

The  $S_2$ -cleavage is kinking or micro-folding followed by some shearing parallel to the limb, whereas the  $S_1$ -cleavage is synchronously sheared parallel to the plane. The mechanism of  $S_1$  and  $S_2$  cleavage formation is revealed in the tectonic movement history in the Rhenohercynian belt of Variscan orogen.

Compared with the observations of Schermer and El-Rus et al., high-pressure metamorphism was created by the result of an A-type subduction, associated with the Rhenohercynian zone as proposed by Weber [60,57,45].

## Conclusions

The present study observed coincidentally the white K-mica by optical petrography of lime-nodule slates from the Lahn-Dill area, Rheinische Schiefergebirge. (i) The confirmation of Phengite mica is carried out by the Mineral chemistry by electron-probe micro-analysis (EPMA) and X-ray powder diffraction (XRPD) analysis. (ii) Phengite Si contents of 3.4 to 3.5 apfu in the celadonite+muscovite solid solution series indicates the pressure 5-6.5 kbars by the Si-isopleths of phengite and the temperature 250-350°C through the lower limit of greenschist and the upper limit of biotite absence. (iii) White K-mica developed in the  $S_2$ -cleavage plane. The  $S_2$ -cleavage cuts at a high angle to the  $S_1$ -cleavage in many places. (iv) The  $S_2$ -cleavage was formed by the high pressure or the Rhenohercynian belt suffered by high-pressure metamorphism due to the buttress of LBM collision. (v) High-pressure metamorphism was created by the result of an A-type subduction, effected within the Rhenohercynian zone. Additionally, the present study would like to recommend a detailed metamorphism of the Rheinische Schiefergebirge gradually died out towards the north for future work.

## Acknowledgments

The authors are deeply indebted to the editor and anonymous reviewers for their constructive and valuable comments and suggestions, which have substantially improved the manuscript. -The first author is greatly indebted to Prof. H. Flick, (Geologisch-Palaeontologisches Institut der Universität Heidelberg) for his guidance. The authors wish to thank Prof. R. O. Greiling (formerly Geologisch-Palaeontologisches Institut der Universität Heidelberg) for the allowance of the measurement of electron microprobe, Dr. H.-P. Meyer (Mineralogisches Institut der Universität Heidelberg) for the measurement and calculation of electron microprobe analysis and Dr. H.-P. Schertl (Institut für Mineralogie, Ruhr-Universität Bochum) for the calculation of data and sharing of knowledge.

## Funding

This research work from the data collection up to the manuscript written has been done by its fund of authors. There are no other means of raising funds.

## Disclosure Statement

No potential conflict of interest was reported by the author.

## References

1. Massonne HJ, Schreyer W. A new experimental phengite barometer and its application to a Variscan subduction zone at the southern margin of the Rhenohercynicum. *Terra cognita*. 1983;3:187.
2. Fladt M, Soder C, Schwarz W, Trieloff M. Petrology and  $^{40}\text{Ar}/^{39}\text{Ar}$ -chronology of metavolcanic rocks from the Northern Phyllite Zone (Southern Hunsrück and Taunus Mountains, Germany): insights into a late Variscan ductile shear zone. *InEGU General Assembly Conference Abstracts*; 2017. 16062p.
3. Anderle HJ, Massonne HJ, Meisl S, Oncken O, Weber K. Southern Taunus Mountains. *InField Guide to Mid German Crystalline Rise and Rheinisches Schiefergebirge (Int. Conf. on Paleozoic Orogens in Central Europe)*; 1990. 125-148p.
4. Röhr C. Petrographic Study of a Paleozoic, Blue Amphibole-and Ferriphengite-bearing Schist from the Southern Taunus Mountains, Germany;2002. [www.oberrheingraben.de/BlueAmph/blueamph.htm](http://www.oberrheingraben.de/BlueAmph/blueamph.htm)
5. Ahrendt H, Clauer N, Hunziker JC, Weber K. Migration of folding and metamorphism in the Rheinische Schiefergebirge deduced from K-Ar and Rb-Sr age determinations. *InIntracontinental fold belts: case studies in the Variscan Belt of Europe and the Damara Belt in Namibia*; 1983. 323-338p.
6. Weber K. Kinematic and metamorphic aspects of cleavage formation in very low-grade metamorphic slates. *Tectonophysics*. 1981;78(1):291-306. [https://doi.org/10.1016/0040-1951\(81\)90018-4](https://doi.org/10.1016/0040-1951(81)90018-4)
7. Kisch HJ. Development of slaty cleavage and degree of very-low-grade metamorphism: a review. *J Metamorph Geol*. 1991;9(6):735-750. <https://doi.org/10.1111/j.1525-1314.1991.tb00562.x>
8. Árkai P, Sassi FP, Desmons J. A systematic nomenclature for metamorphic rocks. 5. Very low-to low-grade metamorphic rocks. Recommendations by the IUGS Subcommission on the systematics of metamorphic rocks. 2007. [www.bgs.ac.uk/scmr/home.html](http://www.bgs.ac.uk/scmr/home.html)
9. Pouchou JL, Pichoir R. Un nouveau modèle de calcul pour la microanalyse quantitative par spectrométrie de rayons X – Partie I: Application à l'analyse d'échantillons homogènes. *La Recherche Aérospatiale*. 1984;3:167-192.
10. Deer WA, Howie RA, Zussman J. An introduction to the rock-forming minerals. Mineralogical Society of Great Britain and Ireland. 2013. <https://doi.org/10.1180/DHZ>
11. Rieder M, Cavazzini G, D'yakonov YS, Frank-Kamenetskii VA, Gottardi G, Guggenheim S. Nomenclature of the micas. *Clay Miner*. 1998;46(5):586-595. <https://doi.org/10.1346/CCMN.1998.0460513>

12. Środoń J, Morgan DJ, Eslinger EV, Eberl DD, Karlinger MR. Chemistry of illite/smectite and end-member illite. *Clay Miner.* 1986;34(4):368-378. <https://doi.org/10.1346/CCMN.1986.0340403>
13. Hunziker JC, Frey M, Clauer N, Dallmeyer RD, Friedrichsen H, Flehmig W. The evolution of illite to muscovite: mineralogical and isotopic data from the Glarus Alps, Switzerland. *Contrib Mineral Petrol.* 1986;92:157-180. <https://doi.org/10.1007/BF00375291>
14. Deer, W. A., Howie, R. A., Zussman, J. Chapter 2. Muscovite and phengite. In *Rock-forming minerals*. Volume 3A. Micas, Fleet, M., Ed., Second Edition. Geological Society of London/UK; 2013b. 41-286p.
15. Ernst WG. Significance of phengitic micas from low-grade schists. *Am Min.* 1963;48(11-12):1357-1373.
16. Park C, Kim N, Choi SJ, Song Y. Mg-phengite in carbonate rock syngenetically formed from hydrothermal fluid: Micro-textural evidence and mineral chemistry. *Minerals.* 2020;10(8):668. <https://doi.org/10.3390/min10080668>
17. Guidotti CV. Muscovite as a petrogenetic indicator mineral in pelitic schists. *Neu Jb Mineral, Abh.* 1976;127:97-142.
18. Torre MD, Livi KJ, Veblen DR, Frey M. White K-mica evolution from phengite to muscovite in shales and shale matrix melange, Diablo Range, California. *Contrib Mineral Petrol.* 1996;123:390-405. <https://doi.org/10.1007/s004100050164>
19. Torre MD, Capitani CD, Frey M, Underwood MB, Mullis J, Cox R. Very low-temperature metamorphism of shales from the Diablo Range, Franciscan Complex, California: New constraints on the exhumation path. *Geol Soc Am Bull.* 1996;108(5):578-601. [https://doi.org/10.1130/00167606\(1996\)108%3C0578:VLTMO%3E2.3.CO;2](https://doi.org/10.1130/00167606(1996)108%3C0578:VLTMO%3E2.3.CO;2)
20. Velde B. Phengite micas; synthesis, stability, and natural occurrence. *Am J Sci.* 1965;263(10):886-913. <https://doi.org/10.2475/ajs.263.10.886>
21. Guidotti CV. 10. Micas In *Metamorphic Rocks*. Micas. 1984:357-468. <https://doi.org/10.1515/9781501508820-014>
22. Frey M. The step from diagenesis to metamorphism in pelitic rocks during Alpine orogenesis. *Sedimentology.* 1970;15(3-4):261-279. <https://doi.org/10.1111/j.1365-3091.1970.tb02189.x>
23. Ehlers, E. G., Blatt, H. *Petrology: Igneous, Sedimentary and Metamorphic*. W. H. Freeman and Co., San Francisco; 1982. 732p.
24. Raudsepp, M., Elisabetta Pani, E., Kern, A. Quantitative Phase Analysis of Sulfide-bearing Mine Wastes Using the Rietveld Method. *International Union of Crystallography*; 2002. 10-12p. [www.iucr.org/iucr-top/comm/cpd/Newsletters/](http://www.iucr.org/iucr-top/comm/cpd/Newsletters/)
25. De Segonzac GD. The transformation of clay minerals during diagenesis and low-grade metamorphism: a review. *Sedimentology.* 1970;15(3-4):281-346. <https://doi.org/10.1111/j.1365-3091.1970.tb02190.x>
26. Kisch HJ. Calibration of the anchizone: a critical comparison of illite 'crystallinity' scales used for definition. *J Metamorph Geol.* 1990;8(1):31-46. <https://doi.org/10.1111/j.1525-1314.1990.tb00455.x>
27. Frey M, Robinson D, editors. *Low-grade metamorphism*. John Wiley & Sons; 2009.
28. Massonne HJ, Schreyer W. Phengite geobarometry based on the limiting assemblage with K-feldspar, phlogopite, and quartz. *Contrib Mineral Petrol.* 1987;96:212-224. <https://doi.org/10.1007/BF00375235>
29. Franz L, Okrusch M, Seidel E, Kreuzer H. Polymetamorphic evolution of pre-Alpidic basement relics in the external Hellenides, Greece. *Neues Jahrbuch für Mineralogie-Abhandlungen.* 2005;181(2):147-172. <https://doi.org/10.1127/0077-7757/2005/0013>
30. Massonne HJ. Metamorphic evolution. In *Pre-Permian geology of central and eastern Europe*; 1995. 132-137p. [https://doi.org/10.1007/978-3-642-77518-5\\_12](https://doi.org/10.1007/978-3-642-77518-5_12)
31. Essene EJ. The current status of thermobarometry in metamorphic rocks. *Geol Soc Spec Publ.* 1989;43(1):1-44. <https://doi.org/10.1144/GSL.SP.1989.043.01.02>
32. Bucher-Nurminen K. A recalibration of the chlorite—biotite—muscovite geobarometer. *Contrib Mineral Petrol.* 1987;96(4):519-522. <https://doi.org/10.1007/BF01166696>
33. Zhu W, Wei C. Thermodynamic modelling of the phengite geobarometry. *Sci. China Series D-Earth Sciences.* 2007;50(7):1033-1039. <https://doi.org/10.1007/s11430-007-0046-4>
34. Holland JG, Lambert RS. Structural regimes and metamorphic facies. *Tectonophysics.* 1969;7(3):197-217. [https://doi.org/10.1016/0040-1951\(69\)90067-5](https://doi.org/10.1016/0040-1951(69)90067-5)
35. Kamzolkin VA, Ivanov SD, Konilov AN. Empirical phengite geobarometer: Background, calibration, and application. *Geol Ore Depos.* 2016;58:613-622. <https://doi.org/10.1134/S1075701516080092>
36. Tilley CE. Some mineralogical transformations in crystalline schists. *Mineral. Mag.* 1926;21(113):34-46. <https://doi.org/10.1180/minmag.1926.021.113.02>
37. Velde B. Upper stability of muscovite. *Am Min.* 1966;51(5-6):924-929.
38. Turner FJ. *Metamorphic petrology: mineralogical and field aspects*. McGraw Hill, London; 1968. 403p.
39. Earle, S. *Physical Geology*. Victoria, B.C.: BC campus. 2015. 718p.
40. Moe A. Structural development of a volcanic sequence of the Lahn area during the Variscan Orogeny in the Rhenohercynian belt (Germany). Doctoral dissertation, Institute of Geology and Palaeontology, Universität Heidelberg; 2000.
41. Martha SO, Zulauf G, Dörr W, Nesbor HD, Petschick R, Prinz-Grimm P, Gerdes A. The Saxothuringian-Rhenohercynian boundary underneath the Vogelsberg volcanic field: evidence from basement xenoliths and U-Pb zircon data of trachyte. *Zeitschrift der deutschen geologischen Gesellschaft.* 2014;165:373-394. <https://doi.org/10.1127/1860-1804/2014/0079>
42. Weber K. Gefügeuntersuchungen an transversalgeschieberten Gesteinen aus dem östlichen Rheinischen Schiefergebirge. *Geol Jahrb D.* 1976;500:15.
43. Hoepfner R. Zum Problem der Bruchbildung, Schieferung und Faltung. *Geol Rundsch.* 1956;45(2):247-283. <https://doi.org/10.1007/BF01802011>
44. Talbot JL. Crenulation cleavage in the Hunsrückschiefer of the Middle Moselle region. *Geol Rundsch.* 1965;54:1026-1043. <https://doi.org/10.1007/BF01820770>
45. [45] Weber, K. The structural development of the Rheinische Schiefergebirge. *Geol mijnb.* 1981b;60(1):149-159.
46. Hedenquist JW, Arribas A. Exploration implications of multiple formation environments of advanced argillic minerals. *Econ Geol.* 2022;117(3):609-643. <https://doi.org/10.5382/econgeo.4880>
47. Lister GS, Snoko AW. SC mylonites. *J Struct Geol.* 1984;6(6):617-638. [https://doi.org/10.1016/0191-8141\(84\)90001-4](https://doi.org/10.1016/0191-8141(84)90001-4)
48. Shimamoto T. The origin of SC mylonites and a new fault-zone model. *J Struct Geol.* 1989;11(1-2):51-64. [https://doi.org/10.1016/0191-8141\(89\)90035-7](https://doi.org/10.1016/0191-8141(89)90035-7)
49. Fossen H. *Structural geology*. Cambridge University Press; 2016. 524p. <https://doi.org/10.1017/9781107415096>
50. Fielitz W. Variscan transpressive inversion in the northwestern central Rhenohercynian belt of western Germany. *J Struct Geol.* 1992;14(5):547-563. [https://doi.org/10.1016/0191-8141\(92\)90156-Q](https://doi.org/10.1016/0191-8141(92)90156-Q)
51. Wrede V, Drozdowski G, Dvorak J. On the structure of the Variscan front in the Eifel-Ardenne area. Rhenohercynian and Subvariscan fold belts. 1993:269-296.
52. Oncken O. Aspects of the reconstruction of the stress history of a fold and thrust belt (Rhenish Massif, Federal Republic of Germany). *Tectonophysics.* 1988;152(1-2):19-40. [https://doi.org/10.1016/0040-1951\(88\)90027-3](https://doi.org/10.1016/0040-1951(88)90027-3)
53. Moe, A. Neotectonic movements in the Rheinisches Schiefergebirge (Germany) and possible rotation. *Zentralblatt für Geologie Paläontologie*; 1999. 81-92p.
54. Wilson CJ. Development of schistosity in phengite schists from Zermatt, Switzerland—discussion. *Tectonophysics.* 1979;56(3-4):305-316. [https://doi.org/10.1016/0040-1951\(79\)90090-8](https://doi.org/10.1016/0040-1951(79)90090-8)
55. Rolland Y, Rossi M, Cox SF, Corsini M, Mancktelow N, Pennacchioni G, et al. 40Ar/39Ar dating of synkinematic white

- mica: insights from fluid-rock reaction in low-grade shear zones (Mont Blanc Massif) and constraints on timing of deformation in the NW external Alps. *Geol Soc Spec Publ.* 2008;299(1):293-315. <https://doi.org/10.1144/SP299.18>
56. Stephens MB, Glasson MJ, Keays R. Structural and chemical aspects of metamorphic layering development in metasediments from Clunes, Australia. *Am J Sci.* 1979;279(2):129-160.
57. El-Rus MA, Khudier AA, Hamid S, Abbas H. The Ampferer-Type Subduction: A Case of Missing Arc Magmatism. In *Updates in Volcanology-Linking Active Volcanism and the Geological Record 2023*. <https://doi.org/10.5772/intechopen.109406>
58. Oncken O, Von Winterfeld C, Dittmar U. Accretion of a rifted passive margin: The Late Paleozoic Rhenohercynian fold and thrust belt (Middle European Variscides). *Tectonics.* 1999;18(1):75-91. <https://doi.org/10.1029/98TC02763>
59. Franke W, Huckriede H, O'Sullivan P, Wemmer K. Zircons to the front: accretionary history of the Rheno-Hercynian active margin (Variscides, Germany). *Can J Earth Sci.* 2019;56(12):1375-1397.
60. Schermer ER. Mechanisms of blueschist creation and preservation in an A-type subduction zone, Mount Olympos region, Greece. *Geology.* 1990;18(11):1130-1133. [https://doi.org/10.1130/0091-7613\(1990\)018%3C1130:MOBCAP%3E2.3.CO;2](https://doi.org/10.1130/0091-7613(1990)018%3C1130:MOBCAP%3E2.3.CO;2)
61. Weber K. Variscan events: early Palaeozoic continental rift metamorphism and late Palaeozoic crustal shortening. *Geol Soc Spec Publ.* 1984;14(1):3-22. <https://doi.org/10.1144/GSL.SP.1984.014.01.02>
62. Die Eidgenössische Technische Hochschule (ETH)-Zürich. The Variscides: An old collisional orogen. *Tectonics*; 2017. <https://www.files.ethz.ch/structuralgeology/jpb/files/english/varisweb.pdf>